In Situ Chemical Characterization of Aged Biomass-Burning Aerosols Impacting Cold Wave Clouds

KERRI A. PRATT,[a,b] ANDREW J. HEYMSFIELD,[c] CYNTHIA H. TWOHY,[d] SHANE M. MURPHY,[e,f] PAUL J. DEMOTT,[g] JAMES G. HUDSON,[h] R. SUBRAMANIAN,[i] ZHIEN WANG,[j] JOHN H. SEINFELD,[e] AND KIMBERLY A. PRATHER[a,k]

[a] *Department of Chemistry and Biochemistry, University of California, San Diego, La Jolla, California*
[c] *National Center for Atmospheric Research, Boulder, Colorado*
[d] *Department of Oceanic and Atmospheric Sciences, Oregon State University, Corvallis, Oregon*
[e] *Division of Chemistry and Chemical Engineering, California Institute of Technology, Pasadena, California*
[f] *Chemical Sciences Division, NOAA/Earth System Research Laboratory, Boulder, Colorado*
[g] *Department of Atmospheric Science, Colorado State University, Fort Collins, Colorado*
[h] *Division of Atmospheric Sciences, Desert Research Institute, Reno, Nevada*
[i] *Droplet Measurement Technologies, Boulder, Colorado*
[j] *Department of Atmospheric Science, University of Wyoming, Laramie, Wyoming*
[k] *Scripps Institution of Oceanography, University of California, San Diego, La Jolla, California*

(Manuscript received 23 September 2009, in final form 21 January 2010)

ABSTRACT

During the Ice in Clouds Experiment–Layer Clouds (ICE-L), aged biomass-burning particles were identified within two orographic wave cloud regions over Wyoming using single-particle mass spectrometry and electron microscopy. Using a suite of instrumentation, particle chemistry was characterized in tandem with cloud microphysics. The aged biomass-burning particles comprised ~30%–40% by number of the 0.1–1.0-μm clear-air particles and were composed of potassium, organic carbon, elemental carbon, and sulfate. Aerosol mass spectrometry measurements suggested these cloud-processed particles were predominantly sulfate by mass. The first cloud region sampled was characterized by primarily homogeneously nucleated ice particles formed at temperatures near −40°C. The second cloud period was characterized by high cloud droplet concentrations (~150–300 cm^{-3}) and lower heterogeneously nucleated ice concentrations (7–18 L^{-1}) at cloud temperatures of −24° to −25°C. As expected for the observed particle chemistry and dynamics of the observed wave clouds, few significant differences were observed between the clear-air particles and cloud residues. However, suggestive of a possible heterogeneous nucleation mechanism within the first cloud region, ice residues showed enrichments in the number fractions of soot and mass fractions of black carbon, measured by a single-particle mass spectrometer and a single-particle soot photometer, respectively. In addition, enrichment of biomass-burning particles internally mixed with oxalic acid in both the homogeneously nucleated ice and cloud droplets compared to clear air suggests either preferential activation as cloud condensation nuclei or aqueous phase cloud processing.

1. Introduction

Biomass-burning emissions represent a considerable source of greenhouse gases and are estimated to contribute ~34%–38% of global carbonaceous aerosol mass (Forster et al. 2007). Particles resulting from biomass burning exert a significant, but uncertain, direct radiative forcing of +0.03 (±0.12) W m^{-2}, which is strongly influenced by aerosol overlying clouds (Chand et al. 2009; Forster et al. 2007). Wildfires also serve as large sources of cloud condensation nuclei (CCN) with a wide range of hygroscopicities (Petters et al. 2009a). Smoke particles acting as CCN have been found to reduce cloud droplet and ice crystal sizes, delaying the onset of precipitation and increasing cloud lifetime (Andreae et al. 2004; Eagan

[b] Current affiliation: Department of Chemistry, Purdue University, West Lafayette, Indiana.

Corresponding author address: Kimberly A. Prather, 9500 Gilman Dr., M/C 0314, La Jolla, CA 92093–0314.
E-mail: kprather@ucsd.edu

DOI: 10.1175/2010JAS3330.1

et al. 1974; Lindsey and Fromm 2008). However, through the semidirect effect, soot absorption may cause evaporation of cloud particles, reducing cloud cover (Ackerman et al. 2000; Lohmann and Feichter 2005). Under different scenarios, Koren et al. (2008) observed smoke particles to either invigorate clouds, increasing cloud fraction and height, or inhibit cloud formation, decreasing cloud fraction and height, depending on the competition between cloud nucleation and aerosol absorption. Wildfires can also be a source of heterogeneous ice nuclei (IN), suggested to be of regional importance based on number concentrations (Petters et al. 2009b; Pueschel and Langer 1973; Twohy et al. 2010).

The chemical composition and associated cloud nucleating properties of smoke particles control their influence on cloud albedo and lifetime. Most studies of biomass-burning aerosols and clouds have focused on air masses near fire sources (e.g., Eagan et al. 1974; Roberts et al. 2003; Vestin et al. 2007). Fresh smoke particles consist of ~80% by mass organic carbon (OC), ~5%–9% black carbon (BC), and ~12%–15% inorganics, such as potassium, sulfate, chloride, and nitrate (Reid et al. 2005). Following emission, aged biomass-burning particles become enriched in sulfate, nitrate, organic acids, and semivolatile organic species (Gao et al. 2003; Reid et al. 2005). The addition of soluble material during aging generally increases the CCN ability of biomass-burning particles (Andreae and Rosenfeld 2008). This aging process may also lower potential IN activity by altering the ice nucleation mechanism from contact freezing to immersion freezing, as assumed in the model simulations of Hoose et al. (2008). However, once smoke plumes undergo atmospheric dilution and particles become altered through significant atmospheric aging, most aerosol characterization methods are limited in the ability to isolate aged biomass-burning particles from aerosols originating from other sources. Thus, there is a lack of observational evidence of the impacts of aged biomass-burning particles on cloud microphysics (Lee et al. 2006).

Using single-particle mass spectrometry and electron microscopy, aged biomass-burning particles were identified within two orographic wave cloud regions over Wyoming during the Ice in Clouds Experiment–Layer Clouds (ICE-L). Using a comprehensive suite of instrumentation, the chemistry of these biomass-burning particles was characterized in detail in tandem with an investigation of the microphysical properties of the studied clouds. A comparison between the cloud residues and surrounding clear-air aerosol particles is provided for size-resolved single-particle chemical composition, nonrefractory aerosol mass concentration, and single-particle black carbon mass concentration data.

2. Experimental design

a. Overview

Measurements of orographic wave clouds and associated clear air, detailed in Table 1, were made aboard the National Science Foundation (NSF)–National Center for Atmospheric Research (NCAR) C-130 aircraft. Herein, we focus on measurements made on 16 December 2007 during research flight 12 (RF12) over Wyoming (43.1°–44.5°N, 106.0°–107.3°W) at 4.7–7.3 km MSL. Carbon monoxide (CO) was measured at 1 Hz using a vacuum ultraviolet resonance fluorescence instrument (Aero-Laser AL5002). An Ultra High Sensitivity Aerosol Spectrometer (UHSAS; Particle Metrics, Inc., Boulder, Colorado) provided submicron aerosol number concentrations (0.1–1.0 μm in diameter). Total condensation nuclei (CN) concentrations were measured using a condensation particle counter (CPC; model 3760, TSI, Inc., Shoreview, MN), detecting particles $>\sim$13 nm in diameter. CCN number concentration measurements were made using the Desert Research Institute (DRI) instantaneous CCN spectrometer (Hudson 1989). A continuous flow diffusion chamber (CFDC) (Eidhammer et al. 2010; Rogers et al. 2001) measured number concentrations of ice-nucleating particles.

Cloud particle size distributions, habits, and phase were measured with a suite of instruments. A two-dimensional optical array cloud probe (2D-C, Particle Measuring Systems, Inc., Boulder, Colorado) was used as the primary measurement of number concentrations of cloud ice crystals >50 μm in diameter. This probe, updated with fast electronics, provided accurate estimates of particle concentrations 50 μm and above as judged by comparison of size distributions measured with a higher-resolution probe, a 2D-S probe, for the first ICE-L flight. The cloud droplet probe (CDP; Droplet Measurement Technologies, Boulder, Colorado) and Forward Scattering Spectrometer Probe (FSSP-100; Particle Measuring Systems Inc.) provided redundant cloud particle size distribution data, mostly cloud drops, in the 1–50-μm-diameter range. The CDP is an open path instrument that is designed to minimize the production of ice artifacts produced by shattering of large ice on the inlet of the probe. The presence and amount of liquid water was derived from the Rosemount icing probe (model 871, Rosemount Engineering Co., Minneapolis, Minnesota) and objectively calibrated using the procedure described in Heymsfield et al. (2005). A cloud particle imager (CPI; Stratton Park Engineering Company Inc., Boulder, Colorado) was used to identify the presence of small ice and large droplets, as well as to identify ice particle habits for sizes above ~40–50 μm. Two Buck Research 1011C cooled mirror hygrometers were used to measure

TABLE 1. List of instruments/techniques utilized with measured parameters and corresponding references noted.

Instrument/technique	Measured parameter(s)	Reference(s)
Aircraft aerosol time-of-flight mass spectrometer (A-ATOFMS)	In situ size and chemical composition of individual particles	Pratt et al. (2009)
Scanning transmission electron microscopy–Energy dispersive X-ray analysis (STEM-EDX)	Size and chemical composition of individual particles	
Aerodyne compact time-of-flight aerosol mass spectrometer (C-ToF-AMS)	In situ aerosol nonrefractory species size-resolved mass concentrations	Drewnick et al. (2005)
Single-particle soot photometer (SP2)	Black carbon mass concentrations	Schwarz et al. (2006); Baumgardner et al. (2008)
Counterflow virtual impactor (CVI)	Separation of cloud droplets and ice crystals from interstitial aerosol	Noone et al. (1988)
Particle Measuring Systems two-dimensional optical array cloud probe (2D-C)	Number concentrations of cloud ice crystals >50 μm	
Droplet Measurement Technologies cloud droplet probe (CDP)	Cloud particle number concentrations (1–50 μm)	
Particle Measuring Systems Forward Scattering Spectrometer Probe (FSSP-100)	Cloud particle number concentrations (1–50 μm)	
Rosemount icing probe	Cloud LWC	
Stratton Park Engineering Company cloud particle imager (CPI)	Cloud particle phase and ice crystal habit identification	
Buck Research 101 1C cooled mirror hygrometers	Water vapor mixing ratio	
MayComm tunable diode laser (TDL) hygrometer	Water vapor mixing ratio and cloud LWC	
Wyoming cloud radar and lidar	Vertical cross sections of cloud particle phase, size, and concentration	Leon et al. (2006); Wang et al. (2009)
Cloud condensation nuclei (CCN) spectrometer	CCN number concentrations	Hudson (1989)
Continuous flow diffusion chamber (CFDC)	Number concentrations of ice-nucleating particles	Rogers et al. (2001); Eidhammer et al. (2010)
Particle Metrics Ultra High Sensitivity Aerosol Spectrometer (UHSAS)	0.1–1.0-μm aerosol number concentrations	
TSI condensation particle counter (CPC)	Total CN number concentrations	
Aero-Laser vacuum ultraviolet resonance fluorescence	Carbon monoxide concentrations	

water vapor mixing ratio. In addition, a MayComm tunable diode laser (TDL) hygrometer was used to measure water vapor mixing ratio and cloud liquid water content (LWC). The Wyoming cloud radar and lidar are airborne remote sensors that provided vertical cross sections from the aircraft to infer properties of cloud particle phase, size, and concentration (Leon et al. 2006; Wang et al. 2009). Vertical velocities were measured with the C-130 aircraft's wind gust probe system.

Cloud residual particles were isolated using a counterflow virtual impactor (CVI) (Noone et al. 1988; Twohy et al. 1997). The CVI separates individual cloud droplets and ice crystals from interstitial aerosol and gases, collecting and concentrating them within a small flow of high-purity dry nitrogen gas heated to 50°C. Cloud particles (droplets and ice crystals) with aerodynamic diameters >6–7 μm were selected using the CVI. Condensed water was evaporated, providing individual residual particles for in situ analysis, described below. Ambient particle impactor samples, described below, were also collected through the CVI inlet by turning off the counterflow, allowing it to function as a simple subisokinetic aerosol inlet. All internal surfaces of the C-130 aircraft CVI inlet were composed of stainless steel. Aerosol and cloud residue chemical composition were measured using real-time mass spectrometry, electron microscopy, and a single-particle soot photometer, described below. For CVI data analysis, time periods were divided into two categories: ice and mixed-phase (i.e., both liquid droplets and ice crystals present simultaneously), corresponding to periods 1 and 2, described in section 3b and in Table 2. To examine the clear air feeding the clouds, time periods with equivalent potential temperatures θ_e of 299.0–306.5 K were chosen based on the θ_e values observed during in-cloud sampling.

b. Aircraft aerosol time-of-flight mass spectrometer

In situ measurements of size-resolved chemical composition of individual submicron particles were made using the recently developed aircraft aerosol time-of-flight mass spectrometer (A-ATOFMS) (Pratt et al. 2009). The A-ATOFMS measures in real time the vacuum

TABLE 2. Cloud microphysical properties for periods 1 and 2 of cloud sampling. Medians, with standard deviations in parentheses, are noted, except for vertical velocity, for which maximum values are reported. Ranges are given for period 2, in which several penetrations were examined.

Property	Period 1	Period 2
2D concentration (L^{-1})	79 (156)	7–18 (3–11)
CDP concentration (cm^{-3})	38 (14)	146–227 (18–82)
FSSP concentration (cm^{-3})	48 (27)	207–335 (12–116)
RICE LWC ($g\ m^{-3}$)	BDL	BDL-0.03 (0.01)
Vertical velocity ($m\ s^{-1}$)	0.69	−0.1 to 2.7
Temperature (°C)	−35.8 (0.2)	−24.1 to −25.2 (0.1–0.7)
θ_e (K)	305.2 (0.2)	298.7–300.6 (0.01–0.7)

aerodynamic diameter d_{va} and dual-polarity mass spectra of individual particles from ~70 to 1200 nm. Following a ^{210}Po neutralizer and pressure-controlled inlet (Bahreini et al. 2008), particles are focused in an aerodynamic lens system. Particles are optically detected by two continuous-wave 532-nm lasers spaced 6.0 cm apart, providing particle velocity and, thus, d_{va}. Polystyrene latex spheres of known physical diameter from 95 to 1500 nm were used for particle size calibration. Particles are desorbed and ionized using 266-nm radiation from a Q-switched neodymium-doped yttrium aluminum garnet (Nd:YAG) laser that operated at ~0.4–0.6 mJ during ICE-L. Positive and negative ions resulting from individual particles are detected within the time-of-flight mass spectrometer. For the analysis discussed herein, 581 individual particles were chemically analyzed: 452 particles during clear-air sampling, 18 during ice CVI sampling, and 111 during mixed phase CVI sampling. Standard errors in particle type number percentages were calculated assuming Poisson statistics. Mass spectral peak identifications correspond to the most probable ions for a given mass-to-charge ratio m/z based on previous laboratory and field studies; the peak area of a specific m/z is related to the amount of a specific species on each particle (Bhave et al. 2002).

c. *Scanning transmission electron microscopy—Energy-dispersive X-ray analysis*

Downstream of the CVI inlet, a two-stage round-jet impactor (Rader and Marple 1985) allowed separation of particles by size. At typical sampling pressures of 500 mb, the small particle impactor plate collected 0.11–0.59-μm geometric diameter d_g unit-density particles; the large particle plate collected larger particles up to several microns in size. Particles were impacted onto transmission electron microscopy (TEM) grids (nickel base coated with formvar and carbon) and were analyzed individually via scanning transmission electron microscopy with energy-dispersive X-ray analysis (STEM-EDX). Analyses were performed on a new Hitachi S-5500 instrument that detected elements down to 6 (carbon) with excellent spectral resolution. Some organic species, in addition to nitrate, volatilize under the vacuum environment of the microscope. Approximately 50–73 particles were randomly selected and analyzed per stage for clear-air and mixed-phase samples. Standard errors of particle type number percentages were calculated based on Poisson statistics.

d. *Compact time-of-flight mass spectrometer*

The Aerodyne compact time-of-flight aerosol mass spectrometer (C-ToF-AMS; Drewnick et al. 2005) measured mass concentrations of nonrefractory species (organics, sulfate, nitrate, ammonium, and a fraction of chloride) in real time. Following a pressure-controlled inlet (Bahreini et al. 2008), ~50–800-nm-d_{va} particles are focused by an aerodynamic lens system, sent through a 3.5% chopper, and then impacted onto a tungsten vaporizer operated at 550°–560°C. Once vaporized, molecules undergo electron impact ionization and are extracted at a rate of ~53 kHz into a time-of-flight mass analyzer. C-ToF-AMS mass loadings were not corrected for collection efficiency (CE; Huffman et al. 2005) because of possible changes in particle phase (Matthew et al. 2008) between clear-air and CVI dry residue sampling. Thus, we are effectively assuming a collection efficiency of 100%, although CE likely varied during the flight with a lower limit of ~24% observed previously for solid ammonium sulfate (Matthew et al. 2008), resulting in possible mass concentration errors of up to a factor of ~4. We report mass fraction ranges based on standard deviations of background filter measurements, as well as variability in the average species mass fractions. Oxygen-to-carbon ratios O/C were calculated following the method of Aiken et al. (2008):

$$\mathrm{O/C} = (0.0382 \pm 0.0005)x + (0.0794 \pm 0.0070), \quad (1)$$

where x is the percentage of organic aerosol mass from m/z 44 (CO_2^+). Fractions of sulfate mass present as sulfuric acid were estimated assuming complete neutralization of ammonium by nitrate and sulfate.

e. *Single-particle soot photometer*

Particles containing black carbon were measured by a single-particle soot photometer (SP2; Droplet Measurement Technologies), a laser-induced incandescence instrument described previously by Schwarz et al. (2006) and Baumgardner et al. (2008). During ICE-L, the SP2 measured BC mass in the range of 0.5–10.5 fg BC (0.08–0.22-μm BC mass equivalent diameter); BC particles

greater than ~10.5 fg saturate the incandescence detector. Because of the limited BC mass range, scaling factors to account for the below- and above-detection-limit BC masses could not be generated for the SP2 data. Therefore, we report BC mass in terms of "total incandescent mass" assuming saturated BC masses as 10.5 fg, resulting in an underestimation in the BC mass concentration. The estimated uncertainty in BC mass is ±20% (Baumgardner et al. 2007) apart from the bias due to undersizing of BC masses over 10.5 fg. Standard deviations are noted as uncertainties for BC mass fractions because these variations were greater than ±20%.

3. Results and discussion

a. Chemical characterization of aged biomass-burning aerosols

Hybrid Single-Particle Lagrangian Integrated Trajectory (HYSPLIT) analysis indicated that the air mass feeding the orographic wave clouds had traveled over Idaho and northern Oregon to eastern Wyoming at ~2.5–6.0 km above ground level over the course of ~12–24 h (HYSPLIT model access is available online at http://ready.arl.noaa.gov/HYSPLIT.php). CO concentrations averaging 132 ± 12 ppbv, characteristic of the remote troposphere (Finlayson-Pitts and Pitts 2000), were observed with average total particle number concentrations of 133 ± 47 cm^{-3}. Number concentrations of particles >100 nm in diameter averaged 67 ± 40 cm^{-3}. While aged biomass-burning air masses are often difficult to identify, single-particle chemical composition measurements by STEM-EDX and A-ATOFMS identified high fractions of biomass-burning particles during RF12, despite the lack of a visible forest fire plume observed from the C-130 aircraft. Single particles identified as biomass burning by A-ATOFMS were composed of internally mixed potassium, organic carbon, elemental carbon, and sulfate (Hudson et al. 2004; Silva et al. 1999). Similarly, individual particles identified by STEM-EDX as biomass burning contained potassium and sulfate and often carbon, as observed previously by Liu et al. (2000). During atmospheric aging, biomass-burning particles remain enriched in potassium, allowing use as a tracer for submicron particles (Cachier et al. 1995). These aged biomass-burning particles were spherical in morphology, as shown in Fig. 1, similar to the majority of aged smoke particles observed previously by Pósfai et al. (2003) for a smoldering fire. The exact source of the aged biomass-burning particles could not be identified by satellite imagery because of extensive cloud cover over the northwestern United States. In the western United States, biomass burning is estimated to contribute ~50% of the annual average total carbonaceous aerosol mass concentrations and ~30% of total fine aerosol mass concentrations (Park et al. 2007).

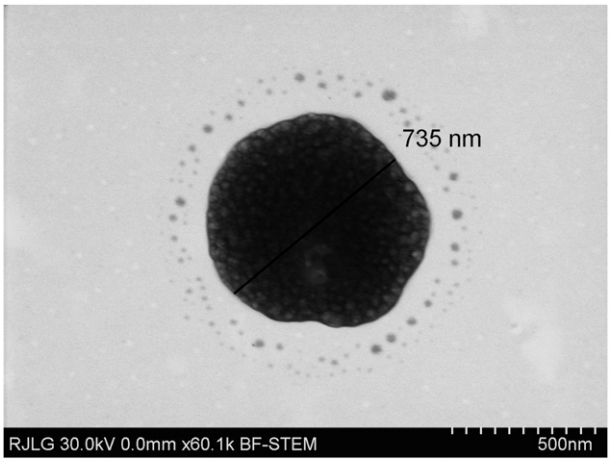

FIG. 1. STEM-EDX image of a 735-nm-diameter aged biomass-burning particle containing carbon, sulfur, oxygen, and potassium.

From the A-ATOFMS data, biomass-burning particles contributed 37 ± 2% by number to the submicron aerosol (d_{va} = 0.1–1.0 μm) (Fig. 2a). This value is in good agreement with STEM-EDX results from the small impactor stage (d_g = 0.11–0.59 μm), showing 26 ± 6% by number to be biomass burning (Fig. 2d); similar results (32 ± 5%) were obtained for the large impactor stage (d_g > 0.59 μm). To examine the chemical mixing state of aged biomass-burning particles, A-ATOFMS digital mass spectra are shown in Fig. 3. Over half of the biomass-burning particles have relatively intense K^+ (m/z 39) signals (area >10 000 arbitrary units), as previously observed by Qin and Prather (2006). Levoglucosan, a degradation product of cellulose, is the most abundant carbohydrate observed in fresh smoke from smoldering fires (5%–14% by mass) (Gao et al. 2003); herein, 33 ± 4% of the aged biomass-burning particles contained levoglucosan ($C_3H_5O_2^+$, m/z −73) (Simoneit et al. 1999). Consistent with the transformation of KCl to K_2SO_4 and KNO_3 during atmospheric aging (Li et al. 2003), only 5 ± 2% of the biomass-burning particles contained chloride (Cl^-, m/z −35); whereas 21 ± 3% and 95 ± 2% contained nitrate (NO_3^-, m/z −62) and sulfate (HSO_4^-, m/z −97), respectively. In addition, several ion markers for potassium–sulfate clusters are present: m/z 175 ($K_2HSO_4^+$), 213 ($K_3SO_4^+$), and −233 [$K(HSO_4)_2^-$]. Ammonium (NH_4^+, m/z 18) and sulfuric acid ($H_2SO_4HSO_4^-$, m/z −195) were internally mixed within 58 ± 4% and 60 ± 4%, respectively, of the biomass-burning particles by number. Oxalic acid ($HC_2O_4^-$, m/z −89), a common secondary organic acid observed for aged biomass-burning particles (Gao et al. 2003), was mixed with 28 ± 3% of the biomass-burning particles.

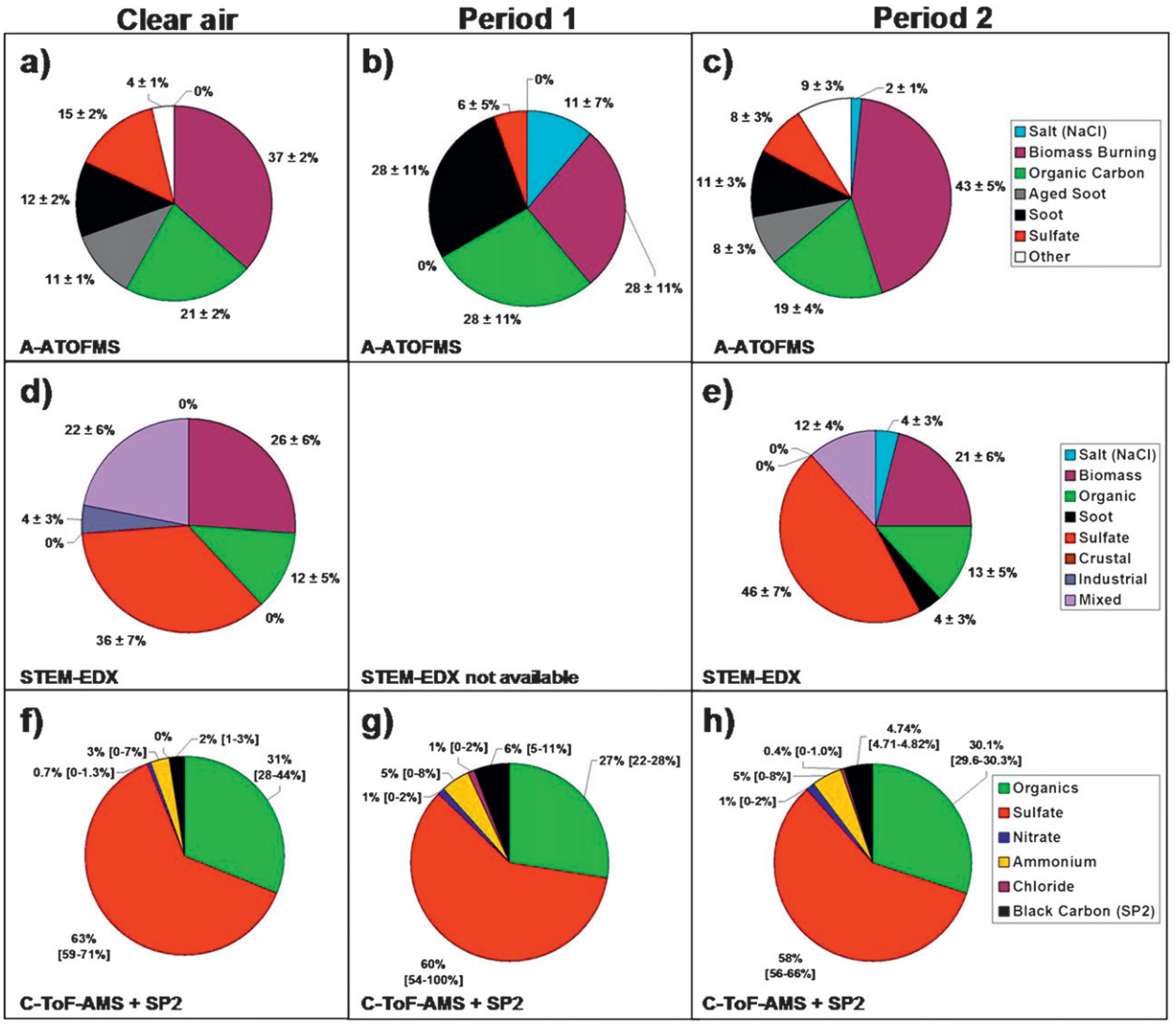

FIG. 2. Summary of clear-air particle and cloud residue chemistry. The columns refer to (a),(d),(f) chemistry of clear-air particles, (b),(g) period 1 cloud residues (likely primarily homogeneously nucleated ice), and (c),(e),(h) period 2 cloud residues (primarily cloud droplets). The rows illustrate the measurements provided by A-ATOFMS, STEM-EDX, and C-ToF-AMS and SP2, as follows: Relative number fractions of particle types were measured by the (a)–(c) A-ATOFMS and (d),(e) STEM-EDX. Uncertainties noted were calculated assuming Poisson statistics for sample sizes of 18–452 particles for the A-ATOFMS and 50–73 particles for the STEM-EDX for each period, as noted in sections 2b and 2c. (f)–(h) Nonrefractory (organics, sulfate, nitrate, ammonium, and chloride) mass fractions measured by the C-ToF-AMS, as well as relative black carbon mass fraction, measured by the SP2. Ranges in C-ToF-AMS mass fractions are based on standard deviations of background filter measurements, as well as sampling variability, and assume a collection efficiency of 1 for the C-ToF-AMS, which introduces additional error, as discussed in section 2d. SP2 mass fraction ranges are based on standard deviations of the ambient measurements, considering the assumptions made for the C-ToF-AMS measurements.

Other particle categories observed by A-ATOFMS included organic carbon, soot, aged soot, sulfate, and other minor types (Fig. 2a). OC particles, contributing 21 ± 2% by number, consisted of internally mixed oxidized OC (e.g., $C_2H_3O^+$, *m*/*z* 43), ammonium, sulfate, and sulfuric acid, showing that these particles were significantly aged, likely primarily through cloud processing (Pratt and Prather 2010). Soot particles, contributing 12 ± 2% by number, were characterized by carbon cluster ions ($C_n^{+/-}$), potassium, sulfate, and sulfuric acid; aged soot particles, contributing 11 ± 1%, included OC markers superimposed on the soot fingerprint, described previously by Moffet and Prather (2009). For STEM-EDX results, soot mixed with sulfate is included within the ''mixed'' particle category, which contributed 22 ± 6% by number. A-ATOFMS particles producing only negative

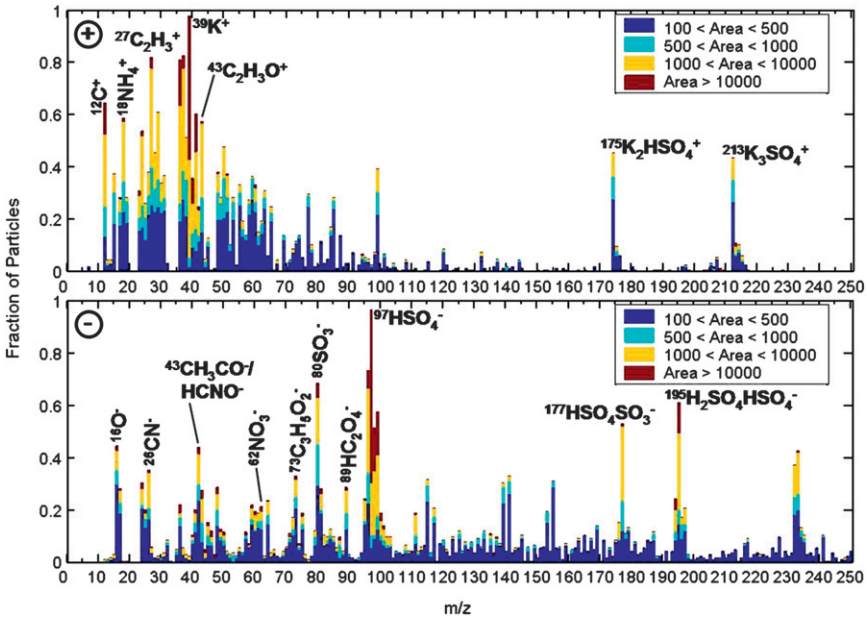

FIG. 3. Positive and negative ion digital mass spectra showing the relative fractions of biomass-burning particles (y axis) containing each m/z (x axis) binned by ion peak area (color scale).

ion mass spectra with sulfate and sulfuric acid ion markers were labeled as externally mixed sulfate particles (Pratt and Prather 2010), which contributed 15 ± 2% by number. Compared to the A-ATOFMS, STEM-EDX showed lower fractions of OC particles (12 ± 5%) and higher fractions of externally mixed sulfate particles (36 ± 7%) for the small impactor stage; however, it is likely that this discrepancy is due to the higher sensitivity of the A-ATOFMS to semivolatile OC, which could volatilize during STEM-EDX analysis. Overall, good agreement was observed between the A-ATOFMS and STEM-EDX particle type number fractions.

Corresponding nonrefractory species (organics, sulfate, nitrate, ammonium, and chloride) and black carbon mass concentrations were measured by the C-ToF-AMS and SP2. Despite the influence of biomass burning, the average total nonrefractory mass concentration of submicron particles ($d_{va} < 1$ μm), or NR-PM$_1$, was only 0.9 μg m^{-3}, with an average black carbon mass concentration of 0.02 μg m^{-3}. Considering the assumption that these instruments measured the bulk of the aerosol mass <1 μm and using a collection efficiency of 1 for the C-ToF-AMS, as outlined in section 2d, mass fractions were calculated. As shown in Fig. 2f, sulfate and organics contributed ~63% and ~31%, respectively, to the submicron aerosol mass, with minor contributions from black carbon (~2%), ammonium (~3%), and nitrate (~0.7%). Compared to fresh smoke (Capes et al. 2008; Reid et al. 2005), significantly higher sulfate mass fractions were observed, likely due to extensive aging and cloud processing of the biomass-burning particles. A-ATOFMS analysis showed 93 ± 1% of all clear-air particles to be internally mixed with sulfate. The C-ToF-AMS sulfate mass mode was measured at a vacuum aerodynamic diameter of ~0.4 μm (not shown), consistent with aged particles. Approximately 76% of the measured nonrefractory sulfate is estimated to be sulfuric acid, considering the relative amounts of ammonium, nitrate, and sulfate present, which is in good agreement with the high number fraction of particles internally mixed with sulfuric acid (68 ± 2%), as measured by A-ATOFMS. In contrast to aged biomass-burning particles internally mixed with nitrate detected in Mexico City by Moffet et al. (2008), the high sulfate and sulfuric acid contents of these aged biomass-burning particles suggests aging primarily through cloud processing (Pratt and Prather 2010).

A marker for levoglucosan mass concentrations, the m/z 60 signal (Alfarra et al. 2007) in the C-ToF-AMS mass spectrum was below detection limits when averaged over all isolated clear-air periods, but m/z 60 was prominently seen above background (not shown) during periods with the highest organic mass loadings, further confirming biomass-burning contributions. In accordance with the low m/z 60 signal, recent laboratory studies indicate that levoglucosan may undergo oxidation during aging (Hoffmann et al. 2010). Previous studies of the aging of biomass-burning aerosols using the Aerodyne

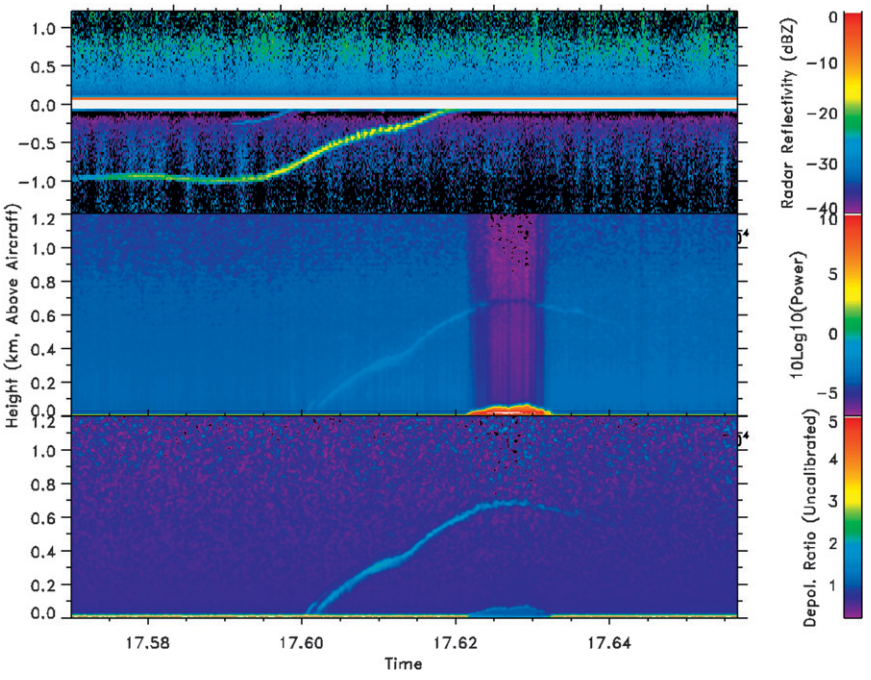

FIG. 4. Period 1 cloud properties, as measured by the Wyoming cloud radar and lidar, with respect to time (h UTC) and altitude (km) of the flight trajectory. (top) Upward- and downward-pointing radar reflectivity (dBZ); the white gap indicates the dead zone near the aircraft. The outline of two ice streamers can be seen in the downward-pointing radar; because of the higher noise level of the upward-pointing radar, the wave clouds above the aircraft cannot be distinguished. (middle) Lidar (upward-pointing) attenuated backscattering power (uncalibrated) and (bottom) lidar linear depolarization ratio (uncalibrated), illustrating the structure of two sampled wave clouds above flight altitude.

AMS have shown organics produced from biomass burning to become more oxygenated with an increasing contribution from m/z 44 compared to m/z 43 (Capes et al. 2008; Grieshop et al. 2009). In agreement, the C-ToF-AMS signal from m/z 44 was greater than m/z 43 for the organics observed during this flight. Further, the measured O/C ratio (0.6 ± 0.1) is consistent with the O/C ratio ($\sim$0.5) of aged organics produced from biomass burning following 5 h of photooxidation (Grieshop et al. 2009).

Overall, the clear air was characterized by aged aerosol particles with biomass-burning particles as the major contributing particle type ($\sim$26%–37% by number) and sulfate, likely in the form of sulfuric acid, as the primary contributor to nonrefractory aerosol mass. The incorporation of these particles into orographic wave clouds is described below.

b. *Orographic wave cloud properties*

Two orographic wave cloud regions, denoted by sampling periods 1 ($\sim$17.57–17.69 h UTC) and 2 ($\sim$18.26–19.09 h UTC), were sampled during RF12. Droplet and ice concentrations, LWC, vertical velocity, temperature, and θ_e are summarized in Table 2 (see Figs. 5 and 6 for temporal profiles of these parameters for representative time periods). During period 1, the C-130 aircraft penetrated two <200-m-thick orographic wave clouds, as revealed by radar and lidar imagery (Fig. 4), formed at temperatures where homogeneous freezing dominates. Figure 5e shows a wavelike pattern consistent with an orographic wave with peak updrafts near 1 m s^{-1} in the region where the relative humidities were highest. Figure 5f shows the thermodynamic structure associated with the wave clouds and clear-air environment. The wave clouds were observed in a thermodynamically stable environment, with θ_e increasing with altitude. No liquid water was detected above the Rosemount icing probe's liquid water detection limit corresponding to $\sim$0.02 g m^{-3} (Fig. 5b).

The first penetration of period 1 at $\sim$17.60 h UTC corresponded to an ice streamer, or wave cloud tail, shown in the lidar imagery (Fig. 4), that was initiated $\sim$700 m above the flight altitude, at a temperature of approximately -44°C. The largest particles observed by the 2D-C probe during this penetration were 150 μm. The ice particles in the streamer were likely in the process of

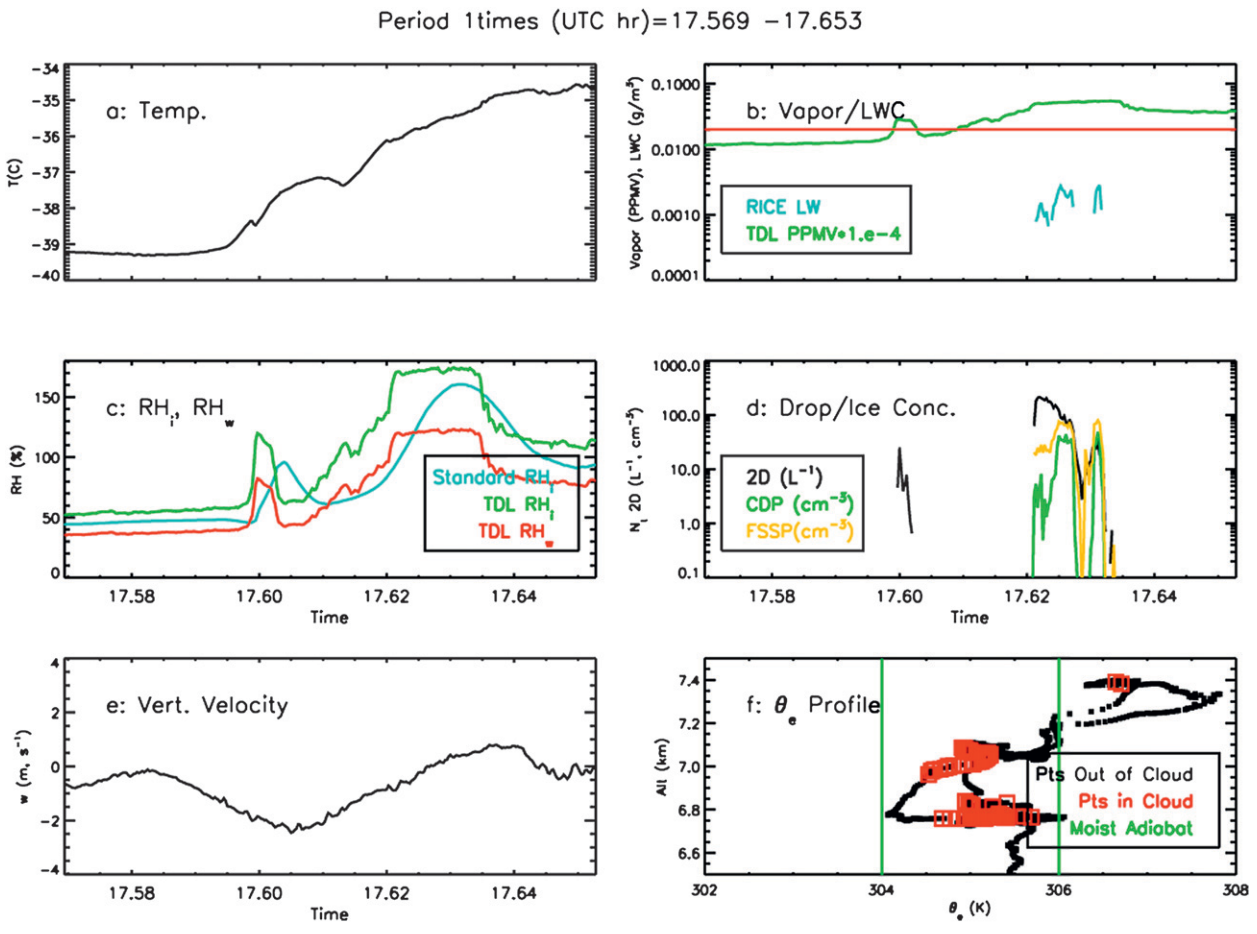

FIG. 5. Period 1 cloud properties: (a) temperature (°C); (b) water vapor content (ppmv) measured by the TDL hygrometer, and cloud LWC (g m^{-3}) measured by the Rosemount icing detector, with the red line denoting the LWC detection limit; (c) RH_i measured by standard and TDL hygrometers, as well as RH_w measured by the TDL hygrometer; (d) cloud particle (droplet–ice) concentrations measured by the following cloud particle probes: 2D (L^{-1}), CDP (cm^{-3}), and FSSP (cm^{-3}); (e) vertical velocity (m s^{-1}); and (f) θ_e (K) with respect to altitude (km) for sampling in and out of cloud with the moist adiabat lines noted.

sublimating because 1) no small particles were detected by the FSSP or CDP (Fig. 5d), 2) the tail was in a region of downdraft, and 3) there was complete sublimation of the ice at ~250 m below flight altitude, as shown by the downward-pointing radar imagery (Fig. 4). If we take the relative humidity with respect to ice RH_i in the cloud tail to be ~100%, we conclude that the TDL hygrometer overestimated RH_i by ~20% at this temperature, whereas the RH_i values measured by the standard two-stage instrument were accurate but with a time lag. Note that the absence of small cloud particles also indicates that the large particles were not contaminating the concentrations measured by the small particle probes. The second penetration at ~17.62–17.63 h UTC corresponded to an ice cloud initiated near flight altitude at a temperature of approximately −37°C. The lidar imagery shows the cloud top extending ~100 m above flight altitude (Fig. 4). The downward-facing radar imagery prior to ~17.62 h UTC shows that these particles formed a long ice streamer, implying a relatively long-lived yet nearly stationary cloud (Fig. 4). The concentrations of >50-μm cloud particles were also relatively high, peaking near 200 L^{-1} (Fig. 5d). Concentrations of <50-μm cloud particles peaked near 50 cm^{-3} for both small particle probes, showing the high concentrations of droplets that froze homogeneously. The observed relatively low lidar linear depolarization ratio (Fig. 4) and small radar reflective factor Z_e indicate the presence of small and spheroid ice crystals from comparison of typical ice crystals at similar temperatures (Wang et al. 2009). The relative humidity was close to water saturation if we subtract 20% from the TDL hygrometer measurements, which is within the measurement error for this RH range, or use the RH from the standard probe with a time lag, as discussed above,

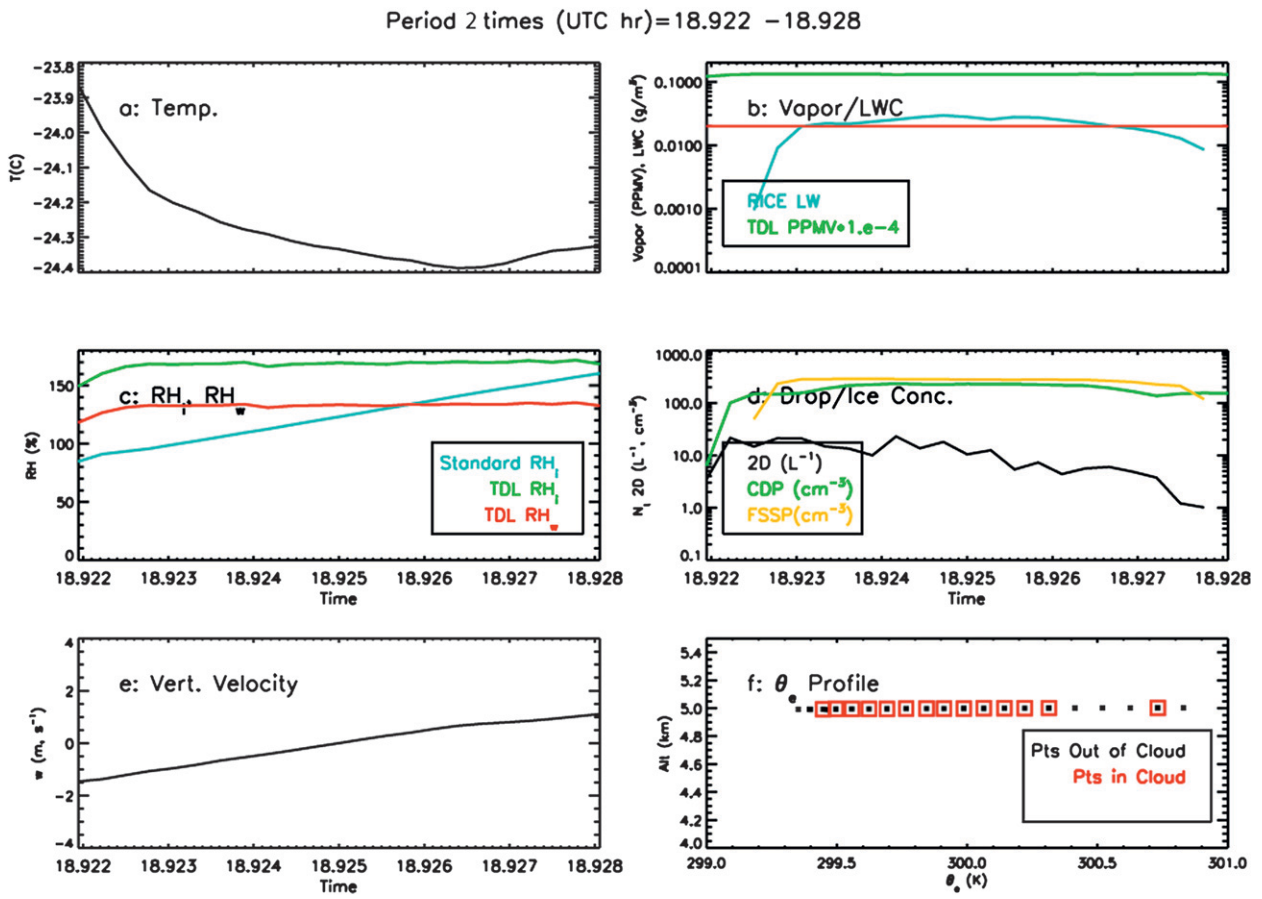

FIG. 6. As in Fig. 5, but for properties of a representative mixed-phase cloud penetration during period 2.

implying that the ice was just in the process of nucleating during this penetration. The high concentrations of small particles were likely depleting the water vapor, yet vertical velocities (maximum 0.7 m s^{-1}) were sufficient to maintain the relatively large RH_i (Fig. 5c). Thus, to summarize, period 1 was characterized by ice formed primarily via homogeneous nucleation with some early development of particles, possibly heterogeneously produced, responsible for the much lower concentration of the largest ice particles observed.

The cloud observed during period 2 was sampled by six penetrations stacked through cloud depth, at temperatures of −24° to −25°C (Table 1). State parameter and microphysical observations for an example penetration are shown in Fig. 6. Radar and lidar imagery (not shown) showed no ice particles feeding into the layer from above or from upwind. The cloud vertical thickness was ~250 m. The values of θ_e were nearly constant through the various cloud penetrations (Table 1) and upwind of them; thus, CCN and IN were feeding into the cloud layer from about the same level as the cloud. Examination of vertical velocity and θ_e profiles showed a stable orographic wave cloud. Droplet concentrations were on average ~150–300 cm^{-3}, with a peak updraft of 2.7 m s^{-1} and maximum LWC of 0.03 g m^{-3}. Given that liquid water contents were relatively low (Table 1 and Fig. 6b), it is not surprising that the mean droplet size, measured by the CDP, was only ~6 μm. Droplet concentrations observed during period 2 were not unusually higher than the small ice concentrations measured during period 1, considering the lower peak vertical velocity (0.7 m s^{-1}) of period 1 compared with period 2 (2.7 m s^{-1}). Average concentrations of ice crystals, measured by the 2D probe, were 7–18 L^{-1}. A brief encounter with 350-μm particles was noted; otherwise, peak particle sizes generated in this thin wave cloud were 250 μm and below. Thus, to summarize, period 2 was characterized primarily by small cloud droplets with a minor contribution from ice crystals formed in situ via heterogeneous freezing.

For an assessment of the CCN efficiency, the fractions of CCN relative to the total CN concentration are plotted versus critical supersaturation S_c, measured by the DRI CCN spectrometer for a portion of the clear-air

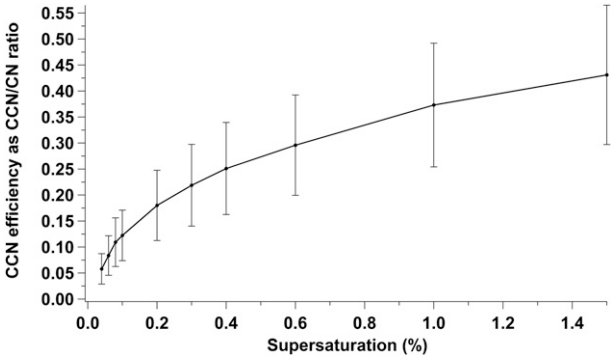

FIG. 7. CCN efficiency, shown as the ratio of CCN to CN, as a function of S_c within the DRI CCN spectrometer measured during a clear-air period from 1756:32 to 1806:54 UTC.

sampling described above (Fig. 7). At 0.6% S_c, a CCN concentration of 46 ± 10 cm^{-3} was measured, which is in agreement with the ICE-L campaign average for clouds at altitudes >6 km (40 cm^{-3}) (Hudson et al. 2010). It is also similar to the number concentration of particles larger than 100 nm in diameter measured by the UHSAS (47 ± 14 cm^{-3}), which corresponds to 30 ± 10% of the total CN concentration. At 1% S_c, 37 ± 12% (58 ± 12 cm^{-3}) of the total CN were estimated to be CCN active, compared to 39% (49 cm^{-3}) for the ICE-L campaign average for clouds at altitudes >6 km (Hudson et al. 2010). The RF12 $CCN_{1\%}$/CN ratio is in agreement with previous measurements of fresh smoke aerosols: $CCN_{1\%}$/CN ratios of 0.24–0.85, depending on fire conditions and fuel type (Hudson et al. 1991). It is important to note, however, that these CCN efficiencies are much higher than previously observed for smoke aerosols produced from burning aviation fuel or crude oil ($CCN_{1\%}$/CN ratios of 0.008–0.07), showing the relative importance of biomass-burning emissions as CCN (Hudson et al. 1991). Since the RF12 measurements are not from within a concentrated biomass-burning plume, it is not surprising that the observed CCN concentrations are more consistent with remote tropospheric conditions (Andreae and Rosenfeld 2008). Further, the observed $CCN_{1\%}$/CN ratios are slightly higher than previously observed over Wyoming in the winter (0.16 ± 0.07) (Delene and Deshler 2001), as might be expected for an air mass influenced by biomass burning. Observed cloud droplet concentrations during period 2 (~150–300 cm^{-3}) are much higher than even the CCN concentrations at 1.5% S_c (67 ± 13 cm^{-3}); however, this discrepancy is likely explained by estimated peak supersaturations with respect to water of ~2%–5% for the observed cold (−24° to −25°C) cloud with relatively high measured vertical velocities (up to 2.7 m s^{-1}) (Heymsfield and Miloshevich 1995). Hudson et al. (2010) noted several instances (11 of 21 clouds) during the ICE-L campaign when droplet concentrations exceeded CCN concentrations at 1.5% supersaturation for high altitude (>6 km) clouds with LWC > 0.01 g m^{-3}.

To estimate the possible contribution of heterogeneous freezing to the large ice concentrations of period 1, IN concentrations were measured by the CFDC during clear-air sampling. The highest IN concentration (considering a 60-s running mean) measured was 8.1 L^{-1} for processing at −32.0°C and a relative humidity with respect to water RH_w of 102.5%. This point suggests that on average ~10% or more of the >50-μm ice particles (average of 79 L^{-1}; Table 1) sampled during period 1 may have formed heterogeneously. In agreement with measured ice concentrations during period 2 (medians of 7–18 L^{-1}; Table 1), IN concentrations reached a 60-s running mean peak of 8.8 L^{-1} for processing at −24.4°C and a relative humidity with respect to water of 103.7%. It should be noted, however, that measured IN concentrations in-cloud behind the CVI were generally less than the measured ice concentrations for RF12, although this discrepancy was not observed by Eidhammer et al. (2010) for a nonbiomass-burning case study. Future efforts will focus on improved closure of these measurements. Across five wave cloud research flights during the ICE-L campaign, Twohy et al. (2010) observed positive correlations between IN concentrations and the number concentrations of soot and biomass-burning particle types. Further, Twohy et al. (2010) observed that the highest IN concentrations measured during ICE-L were within locally produced biomass-burning plumes. Previously, for laboratory-generated smoke aerosols, Petters et al. (2009b) observed ~43% of the fuels tested to produce IN at fractions of 1:10 000 to 1:100 for at least one burn (for CFDC processing at −30°C and water supersaturation conditions), which can impact IN concentrations on a regional scale based on emissions modeling.

To summarize, period 1 was characterized primarily by cloud ice likely formed at −37° and −44°C; ~10% of the observed large ice particles could have undergone heterogeneously freezing with the remainder likely formed via homogeneous freezing. Approximately 24%–42% of the small ice particles were measured during CVI sampling, based on measured residue number concentrations and CDP particle diameters of 4 ± 2 μm, which are less than the CVI cutoff point of ~6–7 μm. In contrast, period 2 was characterized by a mixed-phase cloud at −24° to −25°C dominated by cloud droplets with concentrations of ~150–300 cm^{-3}, suggesting that the particles experienced high supersaturations with respect to water (~2%–5% estimated). A small contribution of heterogeneously nucleated ice (~7–18 L^{-1}) is noted. Based on measured residue number concentrations and

droplet diameters of 6 ± 1 μm for a CVI cutoff point of ~7 μm, ~19%–30% of the droplets were measured during CVI sampling. The chemistry of the ice and mixed-phase residues, with respect to the clear-air particles, is discussed below.

c. Chemical characterization of cloud residues

The chemistry of cloud residues measured during the ice and mixed-phase periods was examined and compared to the clear-air particles. While only a few cloud ice residues were measured by the A-ATOFMS during period 1, an examination of general trends with large estimated uncertainties is presented. For the primarily homogeneously nucleated cloud ice sampled during period 1, 28 ± 11% of the residues were identified as biomass burning by the A-ATOFMS (Fig. 2b), which is similar to clear-air observations (37 ± 2%), suggesting no relative enhancement or depletion in the ice phase. Similarly, OC particles were observed in comparable fractions among the ice residues and clear air (28 ± 11% versus 21 ± 2%). This contrasts measurements of homogeneously frozen cirrus ice residues by Cziczo et al. (2004a,b), wherein potassium- and organic carbon-containing particles preferentially remained in the interstitial aerosol; however, stronger updrafts in the measured clouds favor smaller chemical differences compared to the clear air. In addition, the ICE-L ice residues are suggested to be composed mostly of sulfate based on the high sulfate mass fraction (~60% or greater) estimated for the ice residues (Fig. 2g). Previously, DeMott et al. (2009) examined a lower temperature regime (−45° to −60°C) and observed ice formation by smoke particles as predicted by Koop et al. (2000); however, below we describe a few possible differences between the ice residues and clear-air particles, suggesting a small chemical dependence on freezing.

Soot particles have been previously identified as cirrus ice residues (Petzold et al. 1998; Twohy and Poellot 2005). Among the ice residues sampled in this study, the A-ATOFMS soot particle type contributed 28 ± 11% by number and was observed to be enriched in the ice residues compared to the clear air (12 ± 2%). Similarly, the mass fraction of black carbon, measured by the SP2, was higher for the ice residues compared to the clear air (5%–11% versus 1%–3%, considering uncertainties). A-ATOFMS measurements show that the soot particles were internally mixed with potassium, sulfate, and sulfuric acid, possessing increased hygroscopicity compared to uncoated fresh soot emissions (Lammel and Novakov 1995; Zhang et al. 2008). Previously, the freezing rate of soot-containing droplets has been observed to increase by three orders of magnitude from −34° to −39°C in laboratory experiments, with homogeneous freezing dominating for these particles in this temperature regime (DeMott 1990). Further, at temperatures below −48°C, certain types of sulfuric acid coated soot particles have been observed to nucleate ice at relative humidities below homogeneous freezing thresholds; however, significant differences between different types of soot particles were observed, leading to large uncertainties (Kärcher et al. 2007). It is important to note that soot particles mixed with OC and ammonium sulfate (termed aged soot, described in section 3a) were not observed as cloud ice residues, although they were present in the clear air at a significant fraction (11 ± 1%); however, because of poor statistics for the ice residues, it is unknown whether this difference is significant. Nonetheless, laboratory measurements have noted the ice nucleation ability of some soot particles to be dependent on the coating thickness of OC, with increasing OC contents suppressing water condensation and ice nucleation at ~−66°C (Möhler et al. 2005a); an impedance of homogeneous freezing by organics for smoke particles was also observed recently by DeMott et al. (2009) for temperatures below −50°C. While laboratory measurements of the ice nucleation activity of soot have shown significant dependence on the chemical composition and structural characteristics of soot particles (Koehler et al. 2009), as well as for coatings of organics and sulfuric acid (Möhler et al. 2005b), these effects need to be further characterized to allow an improved comparison with field data. However, herein soot–sulfate particles were observed to be enhanced in the primarily homogeneously nucleated ice, with possible suppression of soot particles internally mixed with organics and ammonium sulfate.

Within the period 1 cloud ice residues, 11 ± 7% by number, measured by the A-ATOFMS, were classified as salts (NaCl), likely sea salt based on chemistry and air mass back trajectories (Pratt et al. 2010). A number higher fraction of cloud ice residues was observed to be internally mixed with chloride compared to the clear air (17 ± 9% versus 3 ± 1%), as measured by the A-ATOFMS. In agreement, the C-ToF-AMS observed a potentially higher mass fraction of nonrefractory chloride for the cloud ice residues compared to the clear air (~1% versus 0%), although poor statistics prohibit further consideration. Since minor fractions of refractory chloride are surface ionized (Allan et al. 2004) by the C-ToF-AMS, the reported mass fractions may be underestimated. As also previously observed by Cziczo et al. (2004a), the enhancement of sea salt among homogeneously nucleated ice residues is likely due to the high solubility and larger diameter of these particles.

Biomass-burning particles internally mixed with levoglucosan were enriched in the ice residues compared

to the clear air (80 ± 18% versus 33 ± 4%), as measured by the A-ATOFMS; however, the m/z 60 signal, a C-ToF-AMS marker for levoglucosan (Alfarra et al. 2007), was below detection limits, showing that this species contributed little to the cloud ice residues by mass due to atmospheric aging, discussed in section 3a. Similarly, the fraction of biomass-burning particles internally mixed with oxalate was higher for the ice residues compared to the clear air (60 ± 22% versus 28 ± 3%), as measured by the A-ATOFMS. In agreement, the contribution of the C-ToF-AMS m/z 44, shown to be correlated with dicarboxylic acids (Takegawa et al. 2007), to the total organic mass was also increased within the ice residues (0.21) compared to the clear air (0.14), although these values are within uncertainties. Pure levoglucosan and oxalic particles have not been shown to effloresce during drying, even at a low relative humidity of 5% (Chan et al. 2005; Prenni et al. 2001). Accordingly, homogeneous freezing of aqueous levoglucosan and oxalic acid particles has been observed during laboratory studies (Knopf and Lopez 2009; Prenni et al. 2001). Zobrist et al. (2006) concluded that liquid droplets containing oxalic acid will nucleate ice homogeneously, unless they contain an oxalic acid dihydrate crystal that would induce freezing at a modestly higher temperature. The enhancement of the fraction of oxalate-containing particles within the ice residues could also be due to production through aqueous cloud processing prior to ice formation (Ervens et al. 2004; Murphy et al. 2006; Sorooshian et al. 2007), as this trend was also observed for the primarily droplet residues sampled during period 2, discussed below.

For anvil cirrus residues, Twohy and Poellot (2005) also observed a decreased abundance of sulfate particles compared to the clear air; however, Heintzenberg et al. (1996) and Cziczo et al. (2004a) observed sulfur preferentially in cirrus residues compared to the interstitial aerosol. During RF12, the contribution of externally mixed sulfate particles was reduced for the cloud ice residues (6 ± 5%) compared to the clear air (15 ± 2%). Biomass-burning particles sampled out of cloud contained higher amounts of potassium sulfate salts in comparison to the biomass-burning ice residues, as shown by the higher (5.5 ± 4.5 times) m/z −233 [$K(HSO_4)_2^-$] peak area, which is proportional to particulate mass. Correspondingly, the mass fraction of nonrefractory sulfate was potentially slightly reduced for the ice residues compared to the clear air (~60% versus ~63%). It should be noted, however, that these sulfate mass fractions are within uncertainties (Fig. 2g); the upper bound uncertainty for the ice residues is an overestimation because it does not account for the presence of other species observed. Further, the fraction of OC particles, measured by the A-ATOFMS, internally mixed with sulfuric acid was significantly reduced for the ice residues compared to the clear air (40 ± 22% versus 86 ± 4%), which is in agreement with a lower estimated contribution of sulfuric acid to the total nonrefractory sulfate mass for the ice residues compared to the clear air (~60% versus ~76%); a smaller difference is observed for the bulk measurement since OC particles represented only ~28% of the total ice residues.

Finally, OC particles measured by the A-ATOFMS in clear air contained higher amounts of oxidized OC in comparison to the OC ice residues, as shown by the higher (3.4 ± 1.5 times) m/z 43 ($C_2H_3O^+$) peak area; it should be noted that this was not observed for all particle types. Previous studies have observed A-ATOFMS m/z 43 to be associated with secondary organic aerosol (X. Qin et al. 2010, unpublished manuscript), which has been observed to have decreased hygroscopicity compared to levoglucosan and oxalic acid, for example, as discussed above (Petters and Kreidenweis 2007). Previous measurements and modeling have also suggested that organics may impede homogeneous freezing (Cziczo et al. 2004b; DeMott et al. 2009; DeMott et al. 2003; Kärcher and Koop 2005; Möhler et al. 2005a). In addition, laboratory studies suggest that certain aqueous organic solutions can form amorphous (noncrystalline, glassy) solids at low temperatures (≤ −43°C) and impede water uptake, ice nucleation, and ice crystal growth (Murray 2008; Zobrist et al. 2008).

The mixed-phase cloud, sampled during period 2, was dominated by cloud droplets because of the relatively low ice concentrations, produced through heterogeneous freezing, as discussed in section 3b. Therefore, the results presented here are likely most representative of cloud droplet properties. Biomass-burning particles were observed to contribute 43 ± 5% by number to the mixed-phase residues, as measured by the A-ATOFMS (Fig. 2c), with large contributions from OC (19 ± 4%) and soot (11 ± 3%) particles. Compared to the A-ATOFMS, STEM-EDX identified a larger fraction of particles as sulfate (46 ± 7% versus 8 ± 3%) and a smaller fraction of particles as biomass burning (21 ± 6% versus 43 ± 5%) for the small impactor stages (Fig. 2e) compared to the large impactor stages (not shown). The electron microscope technique is less sensitive to small contributions of potassium and elemental carbon internally mixed with sulfate, so biomass types may be underestimated.

No significant differences were observed for number fractions of biomass-burning, OC, or soot particle types upon comparison of mixed-phase cloud residues with clear-air particles. While Petters et al. (2009a) observed a range of hygroscopicities κ of 0.02–0.8 for smoke aerosols, it was concluded that most biomass-burning particles do not require atmospheric aging to convert to more

hygroscopic forms to participate in cloud formation. While similar contributions from soot and aged soot particles were observed for mixed-phase cloud residues compared to clear air, the mass fraction of black carbon was slightly higher for mixed-phase residues compared to clear air (~5% versus 1%–3%; Figs. 2f,h). For previous measurements of mixed-phase clouds, black carbon has been shown to be scavenged into the condensed phase to the same extent as the bulk aerosol, which was attributed to a high degree of internal mixing with soluble material (Cozic et al. 2007), as observed in this study.

Biomass-burning mixed-phase residues were observed to be enriched in ammonium [m/z 18(NH_4^+) peak area increased by 2.7 ± 1.5 times] compared to clear-air biomass-burning particles. Previous measurements have shown similar or decreased ammonium mass fractions for droplet residues compared to clear air (Drewnick et al. 2007). Similar to the ice residues, a higher fraction of biomass-burning mixed-phase residues were internally mixed with oxalate compared to clear air (42 ± 7% versus 28 ± 3%), which could be caused by preferential activation as CCN due to the elevated hygroscopicity of oxalic acid compared to most organics (Petters and Kreidenweis 2007; Sun and Ariya 2006) or acquisition of oxalic acid through aqueous cloud processing (Ervens et al. 2004; Sorooshian et al. 2007). Interestingly, the OC mixed-phase residues had higher amine marker ion peak areas [m/z 59 ($C_3H_9N^+$)] (Angelino et al. 2001) compared to clear air (1.8 ± 0.8 times), suggesting increased amine mass concentrations within these particles. Previously, the detection of amines within air masses from a bovine source has been associated with enhanced sub- and supersaturated water uptake (Sorooshian et al. 2008).

Similar to the homogeneously nucleated ice, the contribution of externally mixed sulfate particles was reduced compared to clear air (8 ± 3% versus 15 ± 2%), as measured by the A-ATOFMS; however, STEM-EDX results do not show a significant difference between the mixed-phase residues and clear air for the sulfate particles. C-ToF-AMS results show a slightly decreased sulfate mass fraction for the mixed-phase residues compared to clear air (58 ± 1% versus 63 ± 3%), in addition to a decreased contribution of sulfuric acid to the total sulfate mass (~56% versus ~76%). Previously, Twohy and Anderson (2008) observed a reduced number fraction of sulfate particles within droplet residues compared to clear air; Drewnick et al. (2007) also observed a lower sulfate mass fraction for droplet residues compared to ambient aerosol. The reason for these observations, however, remains unclear based on the hygroscopicity of sulfuric acid and ammonium sulfate in comparison to organics and soot, for example (Petters and Kreidenweis 2007).

4. Conclusions

Biomass-burning particles represent a considerable fraction of global aerosols and thus play a potentially important role in cloud particle formation (Forster et al. 2007). In particular, biomass burning contributes ~50% of the annual average total carbonaceous aerosol mass concentrations and ~30% of total fine aerosol mass concentrations in the western United States (Park et al. 2007). Ambient studies have primarily focused on fresh smoke emissions and their impact on clouds because of the analytical challenge of the identification of aged biomass-burning aerosols. Particle chemical composition evolves with aging, changing the cloud nucleating abilities of particles, highlighting the importance of observational measurements of aged biomass-burning particles and clouds. During research flight 12 of the ICE-L field campaign, aged biomass-burning particles were identified by A-ATOFMS and STEM-EDX. Comprising ~26%–37% by number, the aged biomass-burning particles were characterized by internally mixed potassium, organic carbon, elemental carbon, and sulfate. As measured by the C-ToF-AMS, the majority of the submicron nonrefractory particulate mass was composed of sulfate (~63%) and organics (~31%) with minor contributions from ammonium (~3%) and nitrate (~0.7%); SP2 measurements showed black carbon mass fractions of ~2%. Despite the influence of biomass burning, total NR-PM_1 mass concentrations were 0.9 $\mu g\ m^{-3}$ on average (assuming unity collection efficiency within the C-ToF-AMS) with an average black carbon mass concentration of 0.02 $\mu g\ m^{-3}$ in the clear air. Compared to fresh smoke (Capes et al. 2008; Reid et al. 2005), significantly higher sulfate mass fractions were observed, likely due to extensive aging and cloud processing of the biomass-burning particles.

The aged biomass-burning particles were observed to participate in orographic wave cloud particle formation over Wyoming. During period 1, ice crystals, primarily formed via homogeneous freezing at cloud temperatures of approximately −40°C, were observed at concentrations up to ~50 cm^{-3}. Although only a few cloud ice residues were measured by the A-ATOFMS during period 1, correlations with C-ToF-AMS and SP2 measurements support general trends. The ice residues showed enrichments in the number fraction of soot (mixed with potassium, sulfate, and sulfuric acid), as well as the mass fraction of black carbon, compared to the clear air, suggesting a possible heterogeneous freezing mechanism. In addition, biomass-burning particles internally mixed with levoglucosan or oxalic acid, as well as organic carbon particles internally mixed with sulfuric acid, were observed to be preferentially associated with the ice

residues. The second cloud sampling scenario was characterized by high droplet concentrations (~150–300 cm^{-3}) and low heterogeneously nucleated ice crystal concentrations (~7–18 L^{-1}) at cloud temperatures of −24° to −25°C. For CCN measurements at 1% supersaturation, ~37 ± 12% (58 ± 12 cm^{-3}) of the total CN were estimated to be CCN active; however, higher cloud droplet concentrations were observed, suggesting that high supersaturations with respect to water (up to ~2%–5%) influenced mixed-phase cloud formation. In agreement with the observed high supersaturation, few significant aerosol chemistry differences were observed between the clear-air particles and mixed-phase residues. In particular, biomass-burning particles were not observed to be either enhanced or depleted in the ice or mixed-phase residues. Enrichment of biomass-burning particles internally mixed with oxalic acid in both the homogeneously nucleated ice and cloud droplets suggests either preferential activation as CCN or aqueous phase cloud processing. Future ambient measurements of aged biomass-burning aerosols participating in cold cloud formation are needed to further validate the observed trends. In addition, laboratory measurements of heterogeneous freezing, particularly in the mixed-phase cloud regime, should further examine the impacts of internal mixing with soluble species occurring during atmospheric aging of particles produced during biomass burning. Specifically, chemical composition measurements of the ice nucleating particles resulting from biomass burning must be made to further understand the link between wildfires and heterogeneous ice nucleation.

Acknowledgments. NSF and NCAR are acknowledged for financial support of the ICE-L field campaign, as well as the work of A. J. Heymsfield. K. A. Pratt and K. A. Prather acknowledge NSF for support of ICE-L (ATM-0650659), A-ATOFMS development (ATM-0321362), and a graduate research fellowship for K. A. Pratt. S. M. Murphy and J. H. Seinfeld acknowledge NSF for support of ICE-L (ATM-0340832) and NASA for an Earth and Space Sciences Fellowship for S. M. Murphy. C. H. Twohy, P. J. DeMott, J. G. Hudson, R. Subramanian, and Z. Wang acknowledge NSF for ICE-L support (ATM-0612605, ATM-0611936, ATM-0615414, ATM-0631919, and ATM-0645644, respectively). CVI sampling was performed by Rich Cageo. STEM-EDX analysis was completed by Traci Lersch (RJ LeeGroup, Inc.). Jeffrey R. French and Samuel Haimov (University of Wyoming) assisted with lidar and radar data. Teresa Campos (NCAR) provided carbon monoxide and TDL hygrometer data. Cloud probe data were provided by NCAR/EOL under the sponsorship of NSF (http://data.eol.ucar.edu).

REFERENCES

Ackerman, A. S., O. B. Toon, D. E. Stevens, A. J. Heymsfield, V. Ramanathan, and E. J. Welton, 2000: Reduction of tropical cloudiness by soot. *Science,* **288,** 1042–1047.

Aiken, A. C., and Coauthors, 2008: O/C and OM/OC ratios of primary, secondary, and ambient organic aerosols with high-resolution time-of-flight aerosol mass spectrometry. *Environ. Sci. Technol.,* **42,** 4478–4485.

Alfarra, M. R., and Coauthors, 2007: Identification of the mass spectral signature of organic aerosols from wood burning emissions. *Environ. Sci. Technol.,* **41,** 5770–5777.

Allan, J. D., and Coauthors, 2004: Submicron aerosol composition at Trinidad Head, California, during ITCT 2K2: Its relationship with gas phase volatile organic carbon and assessment of instrument performance. *J. Geophys. Res.,* **109,** D23S24, doi:10.1029/2003JD004208.

Andreae, M. O., and D. Rosenfeld, 2008: Aerosol–cloud–precipitation interactions. Part 1. The nature and sources of cloud-active aerosols. *Earth Sci. Rev.,* **89,** 13–41.

——, ——, P. Artaxo, A. A. Costa, G. P. Frank, K. M. Longo, and M. A. F. Silva-Dias, 2004: Smoking rain clouds over the Amazon. *Science,* **303,** 1337–1342.

Angelino, S., D. T. Suess, and K. A. Prather, 2001: Formation of aerosol particles from reactions of secondary and tertiary alkylamines: Characterization by aerosol time-of-flight mass spectrometry. *Environ. Sci. Technol.,* **35,** 3130–3138.

Bahreini, R., and Coauthors, 2008: Design and operation of a pressure-controlled inlet for airborne sampling with an aerodynamic aerosol lens. *Aerosol Sci. Technol.,* **42,** 465–471.

Baumgardner, D., G. L. Kok, and G. B. Raga, 2007: On the diurnal variability of particle properties related to light absorbing carbon in Mexico City. *Atmos. Chem. Phys.,* **7,** 2517–2526.

——, R. Subramanian, C. Twohy, J. Stith, and G. Kok, 2008: Scavenging of black carbon by ice crystals over the northern Pacific. *Geophys. Res. Lett.,* **35,** L22815, doi:10.1029/2008GL035764.

Bhave, P. V., J. O. Allen, B. D. Morrical, D. P. Fergenson, G. R. Cass, and K. A. Prather, 2002: A field-based approach for determining ATOFMS instrument sensitivities to ammonium and nitrate. *Environ. Sci. Technol.,* **36,** 4868–4879.

Cachier, H., C. Liousse, P. Buat-Menard, and A. Gaudichet, 1995: Particulate content of savanna fire emissions. *J. Atmos. Chem.,* **22,** 123–148.

Capes, G., B. Johnson, G. McFiggans, P. I. Williams, J. Haywood, and H. Coe, 2008: Aging of biomass burning aerosols over West Africa: Aircraft measurements of chemical composition, microphysical properties, and emission ratios. *J. Geophys. Res.,* **113,** D00C15, doi:10.1029/2008JD009845.

Chan, M. N., M. Y. Choi, N. L. Ng, and C. K. Chan, 2005: Hygroscopicity of water-soluble organic compounds in atmospheric aerosols: Amino acids and biomass burning derived organic species. *Environ. Sci. Technol.,* **39,** 1555–1562.

Chand, D., R. Wood, T. L. Anderson, S. K. Satheesh, and R. J. Charlson, 2009: Satellite-derived direct radiative effect of aerosols dependent on cloud cover. *Nat. Geosci.,* **2,** 181–184.

Cozic, J., B. Verheggen, S. Mertes, P. Connolly, K. Bower, A. Petzold, U. Baltensperger, and E. Weingartner, 2007: Scavenging of black carbon in mixed phase clouds at the high alpine site Jungfraujoch. *Atmos. Chem. Phys.,* **7,** 1797–1807.

Cziczo, D. J., D. M. Murphy, P. K. Hudson, and D. S. Thomson, 2004a: Single particle measurements of the chemical composition of cirrus ice residue during CRYSTAL-FACE. *J. Geophys. Res.,* **109,** D04201, doi:10.1029/2003JD004032.

——, and Coauthors, 2004b: Observations of organic species and atmospheric ice formation. *Geophys. Res. Lett.,* **31,** L12116, doi:10.1029/2004GL019822.

Delene, D. J., and T. Deshler, 2001: Vertical profiles of cloud condensation nuclei above Wyoming. *J. Geophys. Res.,* **106,** 12 579–12 588.

DeMott, P. J., 1990: An exploratory study of ice nucleation by soot aerosols. *J. Appl. Meteor.,* **29,** 1072–1079.

——, D. J. Cziczo, A. J. Prenni, D. M. Murphy, S. M. Kreidenweis, D. S. Thomson, R. Borys, and D. C. Rogers, 2003: Measurements of the concentration and composition of nuclei for cirrus formation. *Proc. Natl. Acad. Sci. USA,* **100,** 14 655–14 660.

——, M. D. Petters, A. J. Prenni, C. M. Carrico, S. M. Kreidenweis, J. L. Collett, and H. Moosmüller, 2009: Ice nucleation behavior of biomass combustion particles at cirrus temperatures. *J. Geophys. Res.,* **114,** D16205, doi:10.1029/2009JD012036.

Drewnick, F., and Coauthors, 2005: A new time-of-flight aerosol mass spectrometer (TOF-AMS)—Instrument description and first field deployment. *Aerosol Sci. Technol.,* **39,** 637–658.

——, J. Schneider, S. S. Hings, N. Hock, K. Noone, A. Targino, S. Weimer, and S. Borrmann, 2007: Measurement of ambient, interstitial, and residual aerosol particles on a mountaintop site in central Sweden using an aerosol mass spectrometer and a CVI. *J. Atmos. Chem.,* **56,** 1–20.

Eagan, R. C., P. V. Hobbs, and L. F. Radke, 1974: Measurements of cloud condensation nuclei and cloud droplet size distributions in the vicinity of forest fires. *J. Appl. Meteor.,* **13,** 553–557.

Eidhammer, T., and Coauthors, 2010: Ice initiation by aerosol particles: Measured and predicted ice nuclei concentrations versus measured ice crystal concentrations in an orographic wave cloud. *J. Atmos. Sci.,* **67,** 2417–2436.

Ervens, B., G. Feingold, G. J. Frost, and S. M. Kreidenweis, 2004: A modeling study of aqueous production of dicarboxylic acids: 1. Chemical pathways and speciated organic mass production. *J. Geophys. Res.,* **109,** D15205, doi:10.1029/2003JD004387.

Finlayson-Pitts, B. J., and J. N. Pitts, 2000: *Chemistry of the Upper and Lower Atmosphere: Theory, Experiments, and Applications*. Academic Press, 969 pp.

Forster, P., and Coauthors, 2007: Changes in atmospheric constituents and in radiative forcing. *Climate Change 2007: The Physical Science Basis,* S. Solomon et al., Eds., Cambridge University Press, 129–234.

Gao, S., D. A. Hegg, P. V. Hobbs, T. W. Kirchstetter, B. I. Magi, and M. Sadilek, 2003: Water-soluble organic components in aerosols associated with savanna fires in southern Africa: Identification, evolution, and distribution. *J. Geophys. Res.,* **108,** 8491, doi:10.1029/2002JD002324.

Grieshop, A. P., N. M. Donahue, and A. L. Robinson, 2009: Laboratory investigation of photochemical oxidation of organic aerosol from wood fires. 2: Analysis of aerosol mass spectrometer data. *Atmos. Chem. Phys.,* **9,** 2227–2240.

Heintzenberg, J., K. Okada, and J. Strom, 1996: On the composition of non-volatile material in upper tropospheric aerosols and cirrus crystals. *Atmos. Res.,* **41,** 81–88.

Heymsfield, A. J., and L. M. Miloshevich, 1995: Relative humidity and temperature influences on cirrus formation and evolution: Observations from wave clouds and FIRE II. *J. Atmos. Sci.,* **52,** 4302–4326.

——, ——, C. Schmitt, A. Bansemer, C. Twohy, M. R. Poellot, A. Fridlind, and H. Gerber, 2005: Homogeneous ice nucleation in subtropical and tropical convection and its influence on cirrus anvil microphysics. *J. Atmos. Sci.,* **62,** 41–64.

Hoffmann, D., A. Tilgner, Y. Iinuma, and H. Herrmann, 2010: Atmospheric stability of levoglucosan: A detailed laboratory and modeling study. *Environ. Sci. Technol.,* **44,** 694–699.

Hoose, C., U. Lohmann, R. Erdin, and I. Tegen, 2008: The global influence of dust mineralogical composition on heterogeneous ice nucleation in mixed-phase clouds. *Environ. Res. Lett.,* **3,** 025003, doi:10.1088/1748-9326/3/2/025003.

Hudson, J. G., 1989: An instantaneous CCN spectrometer. *J. Atmos. Oceanic Technol.,* **6,** 1055–1065.

——, J. Hallett, and C. F. Rogers, 1991: Field and laboratory measurements of cloud-forming properties of combustion aerosols. *J. Geophys. Res.,* **96,** 10 847–10 859.

——, S. Noble, and V. Jha, 2010: Comparisons of CCN with supercooled clouds. *J. Atmos. Sci.,* in press.

Hudson, P. K., and Coauthors, 2004: Biomass-burning particle measurements: Characteristic composition and chemical processing. *J. Geophys. Res.,* **109,** D23S27, doi:10.1029/2003JD004398.

Huffman, J. A., J. T. Jayne, F. Drewnick, A. C. Aiken, T. Onasch, D. R. Worsnop, and J. L. Jimenez, 2005: Design, modeling, optimization, and experimental tests of a particle beam width probe for the Aerodyne aerosol mass spectrometer. *Aerosol Sci. Technol.,* **39,** 1143–1163.

Kärcher, B., and T. Koop, 2005: The role of organic aerosols in homogeneous ice formation. *Atmos. Chem. Phys.,* **5,** 703–714.

——, O. Möhler, P. J. DeMott, S. Pechtl, and F. Yu, 2007: Insights into the role of soot aerosols in cirrus cloud formation. *Atmos. Chem. Phys.,* **7,** 4203–4227.

Knopf, D. A., and M. D. Lopez, 2009: Homogeneous ice freezing temperatures and ice nucleation rates of aqueous ammonium sulfate and aqueous levoglucosan particles for relevant atmospheric conditions. *Phys. Chem. Chem. Phys.,* **11,** 8056–8068.

Koehler, K. A., and Coauthors, 2009: Cloud condensation nuclei and ice nucleation activity of hydrophobic and hydrophilic soot particles. *Phys. Chem. Chem. Phys.,* **11,** 7906–7920.

Koop, T., B. P. Luo, A. Tsias, and T. Peter, 2000: Water activity as the determinant for homogeneous ice nucleation in aqueous solutions. *Nature,* **406,** 611–614.

Koren, I., J. V. Martins, L. A. Remer, and H. Afargan, 2008: Smoke invigoration versus inhibition of clouds over the Amazon. *Science,* **321,** 946–949.

Lammel, G., and T. Novakov, 1995: Water nucleation properties of carbon black and diesel soot particles. *Atmos. Environ.,* **29,** 813–823.

Lee, Y. S., D. R. Collins, R. J. Li, K. P. Bowman, and G. Feingold, 2006: Expected impact of an aged biomass burning aerosol on cloud condensation nuclei and cloud droplet concentrations. *J. Geophys. Res.,* **111,** D22204, doi:10.1029/2005JD006464.

Leon, D., G. Vali, and M. Lothon, 2006: Dual-Doppler analysis in a single plane from an airborne platform. *J. Atmos. Oceanic Technol.,* **23,** 3–22.

Li, J., M. Pósfai, P. V. Hobbs, and P. R. Buseck, 2003: Individual aerosol particles from biomass burning in southern Africa: 2. Compositions and aging of inorganic particles. *J. Geophys. Res.,* **108,** 8484, doi:10.1029/2002JD002310.

Lindsey, D. T., and M. Fromm, 2008: Evidence of the cloud lifetime effect from wildfire-induced thunderstorms. *Geophys. Res. Lett.,* **35,** L22809, doi:10.1029/2008GL035680.

Liu, X., P. Van Espen, F. Adams, J. Cafmeyer, and W. Maenhaut, 2000: Biomass burning in southern Africa: Individual particle characterization of atmospheric aerosols and savanna fire samples. *J. Atmos. Chem.,* **36,** 135–155.

Lohmann, U., and J. Feichter, 2005: Global indirect aerosol effects: A review. *Atmos. Chem. Phys.,* **5,** 715–737.

Matthew, B. M., A. M. Middlebrook, and T. B. Onasch, 2008: Collection efficiencies in an Aerodyne Aerosol Mass Spectrometer as a function of particle phase for laboratory generated aerosols. *Aerosol Sci. Technol.,* **42,** 884–898.

Moffet, R. C., and K. A. Prather, 2009: In-situ measurements of the mixing state and optical properties of soot with implications for radiative forcing estimates. *Proc. Natl. Acad. Sci. USA,* **106,** 11 872–11 877.

——, B. de Foy, L. T. Molina, M. J. Molina, and K. A. Prather, 2008: Measurement of ambient aerosols in northern Mexico City by single particle mass spectrometry. *Atmos. Chem. Phys.,* **8,** 4499–4516.

Möhler, O., C. Linke, H. Saathoff, M. Schnaiter, R. Wagner, A. Mangold, M. Kramer, and U. Schurath, 2005a: Ice nucleation on flame soot aerosol of different organic carbon content. *Meteor. Z.,* **14,** 477–484.

——, and Coauthors, 2005b: Effect of sulfuric acid coating on heterogeneous ice nucleation by soot aerosol particles. *J. Geophys. Res.,* **110,** D11210, doi:10.1029/2004JD005169.

Murphy, D. M., and Coauthors, 2006: Single-particle mass spectrometry of tropospheric aerosol particles. *J. Geophys. Res.,* **111,** D23S32, doi:10.1029/2006JD007340.

Murray, B. J., 2008: Inhibition of ice crystallisation in highly viscous aqueous organic acid droplets. *Atmos. Chem. Phys.,* **8,** 5423–5433.

Noone, K. J., J. A. Ogren, J. Heintzenberg, R. J. Charlson, and D. S. Covert, 1988: Design and calibration of a counterflow virtual impactor for sampling of atmospheric fog and cloud droplets. *Aerosol Sci. Technol.,* **8,** 235–244.

Park, R. J., D. J. Jacob, and J. A. Logan, 2007: Fire and biofuel contributions to annual mean aerosol mass concentrations in the United States. *Atmos. Environ.,* **41,** 7389–7400.

Petters, M. D., and S. M. Kreidenweis, 2007: A single parameter representation of hygroscopic growth and cloud condensation nucleus activity. *Atmos. Chem. Phys.,* **7,** 1961–1971.

——, C. M. Carrico, S. M. Kreidenweis, A. J. Prenni, P. J. DeMott, J. L. Collett, and H. Moosmuller, 2009a: Cloud condensation nucleation activity of biomass burning aerosol. *J. Geophys. Res.,* **114,** D22205, doi:10.1029/2009JD012353.

——, and Coauthors, 2009b: Ice nuclei emissions from biomass burning. *J. Geophys. Res.,* **114,** D07209, doi:10.1029/2008JD011532.

Petzold, A., J. Ström, S. Ohlsson, and F. P. Schröder, 1998: Elemental composition and morphology of ice-crystal residual particles in cirrus clouds and contrails. *Atmos. Res.,* **49,** 21–34.

Pósfai, M., R. Simonics, J. Li, P. V. Hobbs, and P. R. Buseck, 2003: Individual aerosol particles from biomass burning in southern Africa: 1. Compositions and size distributions of carbonaceous particles. *J. Geophys. Res.,* **108,** 8483, doi:10.1029/2002JD002291.

Pratt, K. A., and K. A. Prather, 2010: Aircraft measurements of vertical profiles of aerosol mixing states. *J. Geophys. Res.,* D11305, doi:10.1029/2009JD013150.

——, and Coauthors, 2009: Development and characterization of an aircraft aerosol time-of-flight mass spectrometer. *Anal. Chem.,* **81,** 1792–1800.

——, and Coauthors, 2010: Observation of playa salts as nuclei of orographic wave clouds. *J. Geophys. Res.,* **115,** D15301, doi:10.1029/2009JD013606.

Prenni, A. J., P. J. DeMott, S. M. Kreidenweis, D. E. Sherman, L. M. Russell, and Y. Ming, 2001: The effects of low molecular weight dicarboxylic acids on cloud formation. *J. Phys. Chem.,* **105A,** 11 240–11 248.

Pueschel, R. F., and G. Langer, 1973: Sugar cane fires as a source of ice nuclei in Hawaii. *J. Appl. Meteor.,* **12,** 549–551.

Qin, X., and K. A. Prather, 2006: Impact of biomass emissions on particle chemistry during the California Regional Particulate Air Quality Study. *Int. J. Mass Spectrom.,* **258,** 142–150.

Rader, D. J., and V. A. Marple, 1985: Effect of ultra-Stokesian drag and particle interception on impaction characteristics. *Aerosol Sci. Technol.,* **4,** 141–156.

Reid, J. S., R. Koppmann, T. F. Eck, and D. P. Eleuterio, 2005: A review of biomass burning emissions. Part II: Intensive physical properties of biomass burning particles. *Atmos. Chem. Phys.,* **5,** 799–825.

Roberts, G. C., A. Nenes, J. H. Seinfeld, and M. O. Andreae, 2003: Impact of biomass burning on cloud properties in the Amazon Basin. *J. Geophys. Res.,* **108,** 4062, doi:10.1029/2001JD000985.

Rogers, D. C., P. J. DeMott, S. M. Kreidenweis, and Y. Chen, 2001: A continuous-flow diffusion chamber for airborne measurements of ice nuclei. *J. Atmos. Oceanic Technol.,* **18,** 725–741.

Schwarz, J. P., and Coauthors, 2006: Single-particle measurements of midlatitude black carbon and light-scattering aerosols from the boundary layer to the lower stratosphere. *J. Geophys. Res.,* **111,** D16207, doi:10.1029/2006JD007076.

Silva, P. J., D. Y. Liu, C. A. Noble, and K. A. Prather, 1999: Size and chemical characterization of individual particles resulting from biomass burning of local southern California species. *Environ. Sci. Technol.,* **33,** 3068–3076.

Simoneit, B. R. T., J. J. Schauer, C. G. Nolte, D. R. Oros, V. O. Elias, M. P. Fraser, W. F. Rogge, and G. R. Cass, 1999: Levoglucosan, a tracer for cellulose in biomass burning and atmospheric particles. *Atmos. Environ.,* **33,** 173–182.

Sorooshian, A., M.-L. Lu, F. J. Brechtel, H. Jonsson, G. Feingold, R. C. Flagan, and J. H. Seinfeld, 2007: On the source of organic acid aerosol layers above clouds. *Environ. Sci. Technol.,* **41,** 4647–4654.

——, and Coauthors, 2008: Comprehensive airborne characterization of aerosol from a major bovine source. *Atmos. Chem. Phys.,* **8,** 5489–5520.

Sun, J. M., and P. A. Ariya, 2006: Atmospheric organic and bioaerosols as cloud condensation nuclei (CCN): A review. *Atmos. Environ.,* **40,** 795–820.

Takegawa, N., T. Miyakawa, K. Kawamura, and Y. Kondo, 2007: Contribution of selected dicarboxylic and ω-oxocarboxylic acids in ambient aerosol to the m/z 44 signal of an Aerodyne Aerosol Mass Spectrometer. *Aerosol Sci. Technol.,* **41,** 418–437.

Twohy, C. H., and M. R. Poellot, 2005: Chemical characteristics of ice residual nuclei in anvil cirrus clouds: Evidence for homogeneous and heterogeneous ice formation. *Atmos. Chem. Phys.,* **5,** 2289–2297.

——, and J. R. Anderson, 2008: Droplet nuclei in non-precipitating clouds: composition and size matter. *Environ. Res. Lett.,* **3,** 045002, doi:10.1088/1748-9326/3/4/045002.

——, A. J. Schanot, and W. A. Cooper, 1997: Measurement of condensed water content in liquid and ice clouds using an airborne counterflow virtual impactor. *J. Atmos. Oceanic Technol.,* **14,** 197–202.

——, and Coauthors, 2010: Relationships of biomass-burning aerosols to ice in orographic wave clouds. *J. Atmos. Sci.,* **67,** 2437–2450.

Vestin, A., J. Rissler, E. Swietlicki, G. P. Frank, and M. O. Andreae, 2007: Cloud-nucleating properties of the Amazonian biomass burning aerosol: Cloud condensation nuclei measurements

and modeling. *J. Geophys. Res.,* **112,** D14201, doi:10.1029/2006JD008104.

Wang, Z., P. Wechsler, W. Kuestner, J. French, A. Rodi, B. Glover, M. Burkhart, and D. Lukens, 2009: Wyoming Cloud Lidar: Instrument description and applications. *Opt. Express,* **17,** 13 576–13 587.

Zhang, R., A. F. Khalizov, J. Pagels, D. Zhang, H. Xue, and P. H. McMurry, 2008: Variability in morphology, hygroscopicity, and optical properties of soot aerosols during atmospheric processing. *Proc. Natl. Acad. Sci. USA,* **105,** 10 291–10 296.

Zobrist, B., and Coauthors, 2006: Oxalic acid as a heterogeneous ice nucleus in the upper troposphere and its indirect aerosol effect. *Atmos. Chem. Phys.,* **6,** 3115–3129.

——, C. Marcolli, D. A. Pedernera, and T. Koop, 2008: Do atmospheric aerosols form glasses? *Atmos. Chem. Phys.,* **8,** 5221–5244.